Journal of Petroleum Science and Engineering, manuscript No. 2210

Cross-hole electromagnetic and seismic modeling for CO_2 detection and monitoring in a saline aquifer

Short title: EM and seismic modeling for CO_2 detection

José M. Carcione[a] · Davide Gei[a] · Stefano Picotti[a] · Alberto Michelini[b]

Carcione, José M., Gei, Davide, Picotti, Stefano, Michelini,Alberto, Cross-hole electromagnetic and seismic modeling for CO2 detection and monitoring in a saline aquifer, Journal of Petroleum Science and Engineering (2012), doi:10.1016/j.petrol.2012.03.018. Received: 23/07/2011 – Accepted: 15/03/2012

Abstract The injection of CO_2 in saline aquifers and depleted hydrocarbon wells is one solution to avoid the emission of that greenhouse gas to the atmosphere. Carbon taxes can be avoided if geological sequestration can efficiently be performed from technical and economic perspectives. For this purpose, we present a combined rock-physics methodology of electromagnetic (EM) and seismic wave propagation for the detection and monitoring of CO_2 in crosswell experiments.

First, we obtain the electrical conductivity and seismic velocities as a function of saturation, porosity, permeability and clay content, based on the CRIM and White models, respectively. Then, we obtain a conductivity-velocity relation. This type of relations is useful when some rock properties can be more easily measured than other properties. Finally, we compute crosswell EM and seismic profiles using direct modeling techniques. P- and S-wave attenuation is included in the seismic simulation by means of

[a]Istituto Nazionale di Oceanografia e di Geofisica Sperimentale (OGS), Borgo Grotta Gigante 42c, 34010 Sgonico, Trieste, Italy. E-mail: jcarcione@inogs.it

[b]Istituto Nazionale di Geofisica e Vulcanologia (INGV), Via di Vigna Murata, 605, 00143 Roma, Italy. E-mail: alberto.michelini@ingv.it

White's mesoscopic theory. The modeling methodology is useful to perform sensitivity analyses and it is the basis for performing traveltime EM and seismic tomography and obtain reliable estimations of the saturation of carbon dioxide. In both cases, it is essential to correctly pick the first arrivals, particularly in the EM case where diffusion wavelength is large compared to the source-receiver distance.

The methodology is applied to CO_2 injection in a sandstone aquifer with shale intrusions, embedded in a shale formation. The EM traveltimes are smaller after the injection due to the higher resistivity caused by the presence of carbon dioxide, while the effect is opposite in the seismic case, where water replaced by gas decreases the seismic velocity.

Keywords Electromagnetic modeling · Seismic modeling · CO_2 detection.

1 Introduction

Geological sequestration is an immediate option to solve in part the problem of carbon-dioxide emission to the atmosphere. Feasible possibilities are injection into hydrocarbon reservoirs and and saline aquifers (Arts et al., 2004; Carcione et al., 2006; Alavian and Whitson, 2011). It is essential in CO_2 sequestration to monitor the injected plumes as they diffuse into the reservoir, and any leakage has to be carefully monitored. The loss of integrity of the cap rock above the reservoir and the potential for leakage along bedding planes, faults and fractures should be detected. Seismic and electromagnetic (EM) methods can be used for non-invasive determination of subsurface physical and chemical properties (Giese et al., 2009). Seismic measurements provide P- and S-wave velocities and attenuations, while electromagnetic data at low frequencies provide electrical conductivity, which can be related to fluid saturation. The combined use of these methods can give more reliable results if the interpretation is based on suitable cross-property relations between seismic velocity and conductivity (Carcione et al., 2007). In particular, the electrical conductivity of reservoir rocks is highly sensitive to changes in water and CO_2 saturation and on a lesser degree the P-wave velocity, while the S-wave velocity remains nearly constant.

A few authors have used EM methods to monitor CO_2 in the underground. Norman et al. (2008) built a resistivity model from seismic data and Archie's law. The time-lapse responses for the 2001 and 2006 plumes at Sleipner versus the case without CO_2 indicate peak anomalies of 25 % and 50 % at 3 km offset respectively. Bourgeois et al. (2009) performed a feasibility study of monitoring a supercritical CO_2 injection in a deep saline aquifer by means of EM methods, where the source is a deep metallic casing.

Hoversten et al. (2004) performed crosswell seismic and EM imaging to produce a velocity tomogram and a conductivity section to derive porosity and water saturation. They found a poor petrophysical relationship between velocity and porosity, clay content, and water saturation, but strong petrophysical relations between electrical conductivity and these parameters. In Hoversten et al. (2006), the authors link reservoir parameters to geophysical parameters through a rock-properties model. The adopted model is the Hertz-Mindlin contact theory for the dry frame and modified Hashin-Shtrikman lower bounds to calculate the effective moduli. On the other hand, Archie's law is used to model electrical resistivity as a function of porosity and water saturation. Lei and Xue (2009) performed laboratory measurements at ultrasonic frequencies during the injection of CO_2 into a water-saturated sandstone sample. CO_2 migration and water displacement were mapped using tomographic images of velocity and quality factor. On average, the P-wave velocity deceased by 7.5, 12, and 14.5 % and the inverse quality factor increased by factors of 3.3, 2.7, and 3.7 as a result of the replacement of water with CO_2 during the injection of gaseous, liquid, and supercritical CO_2, respectively. Both the velocity and attenuation data were in good agreement with White's model used in the present work.

Electrical resistivity tomography (ERT) in crosswell configurations is another technique being employed for detecting CO_2. Christensen et al. (2006) have shown the potential of ERT to detect the resistivity changes caused by CO_2 injection and migration in geological reservoirs. Recently, Hagrey (2010) performed an ERT crosswell numerical study and showed that the method can discriminate the various components of a CO_2 storage in conductive saline reservoirs, namely, the plume, the host reservoir, and the cap rock.

In this work, we deal with transient fields that can be processed to obtain the electrical conductivity with crosshole experiments (e.g., Wilt et al., 1995). We use the White/CRIM relation between seismic velocity and electrical conductivity, which has been successfully tested with well-log data of the North Sea (Carcione et al., 2007). This relation provides a reasonable fit to the data, indicating that it is possible to predict an electrical property from an elastic property and vice versa. Then, we perform a sensitivity analysis by computing the EM field and synthetic seismograms corresponding to a geological model of CO_2 partial saturation, based on a cross-hole source-receiver configuration. Finally, we obtain traveltime picks (first arrival versus receiver locations) which are the basis for EM and seismic tomography.

2 The cross-property relation between conductivity and seismic velocity

The key property to relate the electrical conductivity to the P- and S-wave velocities is the porosity. Assume that the conductivity and velocity have the form $\sigma = f(\phi)$ and $v = g(\phi)$, where ϕ is the porosity. Then, the relation is given by $\sigma = f[g^{-1}(v)]$. This simple 1D concept is quite general and can be applied to higher spatial dimensions and the case of anisotropy (e.g., Kachanov et al., 2001; Carcione et al., 2007).

2.1 Electromagnetic properties. CRIM model

The complex refractive index method (CRIM) for a shaly sandstone with negligible permittivity and partially saturated with gas, can be expressed as

$$\sigma = \left[(1-\phi)(1-C)\sigma_q^\gamma + (1-\phi)C\sigma_c^\gamma + \phi(1-S_g)\sigma_b^\gamma + \phi S_g \sigma_g^\gamma\right]^{1/\gamma}, \quad \gamma = 1/2 \quad (1)$$

(Schön, 1996; Carcione et al., 2007; Carcione, 2007), where σ_q, σ_c, σ_b and σ_g are the sand-grain (quartz), clay, brine and gas conductivities, C is the clay content, and S_g is the gas saturation. If γ is a free parameter, the equation is termed Lichtnecker-Rother formula. It is based on the ray approximation. The travel time in each medium is inversely proportional to the electromagnetic velocity, which in turn is inversely proportional to the square root of the complex dielectric constant. At low frequencies, displacement currents can be neglected and equation (1) is obtained. Generally $\sigma_q = \sigma_g = 0$ and equation (1) becomes

$$\sigma = \left[(1-\phi)C\sigma_c^\gamma + \phi(1-S_g)\sigma_b^\gamma\right]^{1/\gamma}, \quad \gamma = 1/2. \quad (2)$$

For zero clay content, equation (2) is exactly Archie's law used in Hoversten et al. (2006).

2.2 Elastic properties. White model

The seismic velocities and quality factors are determined from a mesoscopic rock-physics theory (White, 1975), which provides realistic values as a function of porosity, gas saturation, clay content, fluid viscosity and permeability (Appendix A). It is assumed that the medium has patches of CO_2 in a brine saturated background, where brine has absorbed the maximum amount of CO_2. White's model (see Carcione et al., 2003) describes wave velocity and attenuation as a function of frequency. We introduce shear dissipation as indicated in Appendix A, and for a given reference frequency, f_0, which is the dominant source frequency, we obtain the P- and S-wave phase velocities. The model depends on the patch size r_0. White assumed spherical gas pockets much larger than the grains but much smaller than the wavelength. He developed the theory for a gas-filled sphere of porous medium of radius r_0 located inside a water-filled cube of porous medium. For simplicity in the calculations, White considered an outer sphere of radius r_1 ($r_1 > r_0$), instead of a cube, where $S_g = r_0^3/r_1^3$. More details can be found in White (1975), Carcione et al. (2003) and Carcione (2007).

For homogeneous waves in isotropic media, the phase velocity and attenuation factors are given by

$$v_p = \left[\mathrm{Re}\left(\frac{1}{v}\right)\right]^{-1} \quad \text{and} \quad \alpha = -\omega \mathrm{Im}\left(\frac{1}{v}\right), \tag{3}$$

respectively, where v denotes the complex velocity of the wave mode, and ω is the angular frequency $\omega = 2\pi f$. The corresponding quality factor is

$$Q = \frac{\mathrm{Re}(v^2)}{\mathrm{Im}(v^2)}, \tag{4}$$

and the quality factor associated with White bulk modulus K is

$$\frac{\mathrm{Re}(K)}{\mathrm{Im}(K)}. \tag{5}$$

The P- and S-wave complex velocities of the partially saturated porous medium are

$$v_P = \sqrt{\frac{1}{\rho}\left(K + \frac{4}{3}\boldsymbol{\mu}\right)} \quad \text{and} \quad v_S = \sqrt{\frac{\boldsymbol{\mu}}{\rho}}, \tag{6}$$

respectively, where $\boldsymbol{\mu}$ is the shear complex modulus of the matrix as given in Appendix A [equation (21)]. The density of the medium is

$$\rho = (1-\phi)[(1-C)\rho_q + C\rho_c] + \phi\rho_f, \tag{7}$$

where ρ_q and ρ_c are the sand-grain (quartz) and clay densities, respectively, and

$$\rho_f = S_g \rho_g + (1 - S_g)\rho_b \tag{8}$$

is the density of the gas-liquid mixture, where ρ_g and ρ_b are the gas and brine densities, respectively.

The presence of clay modifies the effective bulk and shear moduli of the grains, K_s and μ_s. That is, the grains are formed by a mixture of quartz and clay. We assume that this moduli are equal to the arithmetic average of the upper and lower Hashin-Shtrikman bounds (Hashin and Shtrikman, 1963; Mavko et al., 1998).

The bulk modulus of the matrix is obtained by using Krief model. A suitable expression is

$$K_m = K_s (1 - \phi)^{\mathcal{A}/(1-\phi)}, \tag{9}$$

where $\mathcal{A}$ is a dimensionless parameter which depends on the pore shape and Poisson ratio of the matrix. This parameter is a pore compliance coefficient, and takes a value of about 2 for spherical pores, increasing as the pores become more crack-like (Le Ravalec and Gueguen, 1996; David and Zimmerman, 2011). We assume the dry-rock shear modulus

$$\mu_m = \frac{\mu_s}{K_s} K_m. \tag{10}$$

This relation implies that the Poisson ratio of the dry porous rock is equal to the Poisson ratio of the mineral forming the rock frame. This is generally not the case (Le Ravalec and Gueguen, 1996; David and Zimmerman, 2011), but that simplification is used in the absence of data to calibrate the model. An alternative model, based on the DEM theory (Li and Zhang, 2011), can be used if one has information about the dominant aspect ratio of the pores. In a real situation, one could evaluate the dry-rock moduli from the wet-rock moduli obtained from sonic-log data (by using the inverse

Gassmann's equations), or obtain those moduli from cores by measuring the P- and S-wave velocities in the laboratory.

As mentioned above, to relate the velocities to the conductivities, we replace $\phi = \phi(\sigma)$ [taken from equation (1)] into equations (6), where

$$\phi(\sigma) = \frac{\sigma^\gamma - (1-C)\sigma_q^\gamma - C\sigma_c^\gamma}{(1-S_g)\sigma_b^\gamma + S_g\sigma_g^\gamma - (1-C)\sigma_q^\gamma - C\sigma_c^\gamma}, \quad (\gamma = 1/2 \ \ \text{CRIM}). \tag{11}$$

3 Modeling methods

3.1 Electromagnetic modeling

The modeling method to compute diffusion fields is that of Carcione (2006, 2007, 2010), who proposed a spectral algorithm to solve the electromagnetic diffusion equation. Let us assume that the material properties and the source are invariant in the y-direction. Then, the propagation can be described in the (x, z)-plane, and E_x, E_z and H_y are decoupled from E_y, H_x and H_z, corresponding to the so-called TM (transverse magnetic) and TE (transverse electric) equations, where E and H denote electric and magnetic fields, respectively. The TM equation is

$$\mu_0 \dot{H}_y = (\sigma^{-1} H_{y,x})_{,x} + (\sigma^{-1} H_{y,z})_{,z} - \mu_0 \dot{M}_y + (J_{x,z} - J_{z,x}). \tag{12}$$

where μ_0 is the magnetic permeability of vacuum and M_y and J are magnetic and electric sources, respectively. A dot above a variable denotes time differentiation, and the subindices $,x$ and $,z$ indicate spatial derivatives with respect to the Cartesian coordinates. Electric-field components can be computed by using Maxwell's equations,

$$\begin{pmatrix} E_x \\ E_z \end{pmatrix} = \frac{1}{\sigma} \begin{pmatrix} -\partial_z H_y \\ \partial_x H_y \end{pmatrix}. \tag{13}$$

The algorithm uses an explicit scheme based on a Chebyshev expansion of the evolution operator, and the spatial derivatives are computed with a pseudospectral method, which allows the use of coarser grids compared to finite-difference methods (see Appendix B) . The modeling allows general material variability and provides snapshots and time histories of the electric and magnetic fields.

3.2 Seismic modeling

The synthetic seismograms are computed with a modeling code based on an isotropic and viscoelastic stress-strain relation. The equations are given in Section 3.9 of Carcione (2007) and were first introduced by Carcione et al. (1988) (see Appendix C). The algorithm is based on the Fourier pseudospectral method for computing the spatial derivatives and a 4th-order Runge-Kutta technique for calculating the wavefield recursively in time.

The wave equation and propagation properties are given in Appendix C, where it is shown how to obtain the viscoelastic parameters. Shear loss is modeled as indicated in the appendices, where a viscoelastic extension of White's theory has been performed.

4 Examples and simulations

The properties of the shaly sandstone are given in Table 1. Figure 1 shows the conductivity σ as a function of the gas saturation S_g and clay content C. As expected, decreasing conductivity is associated with increasing gas saturation, as well as decreasing clay content.

Table 1

Figure 1

The P-wave and S-wave velocities at $f_0 = 200$ Hz are displayed in Figure 2 as a function of gas saturation and different values of clay content. $\mathcal{A} = 3$ is used in equation (9). The velocities have a minimum value depending on the clay content. The velocity increase with clay at a fixed low saturation is due to the fact that a small amount of clay induces a substantial decrease in permeability in the range C = [5,10] %, and this generates a rock stiffening, i.e., White's bulk modulus increases. This poroelastic effect mainly affects factor W (see equation (16)). However, the dominant trend is a velocity decrease due to the substitution of brine by gas, while beyond that range fluid density effects are more important and the velocities increase. The density effects affect the whole range of saturations in the S-wave velocity. Generally, when the clay content increases the velocities decrease as expected.

Figure 2

Next, we analyze the cross-property relation between velocity and conductivity. We consider well-log data of the Gullfaks field in the North Sea. The well is vertical and consists of sand and shale filled with brine. The velocity-conductivity relation is shown in Figure 3, where the numbers correspond to the clay content. The curves show a good agreement with the data. Figure 4 shows the cross-property relation between the wave velocities and the conductivity for $S_g = 0.1$ and $S_g = 0.4$. Higher velocity is associated with lower conductivity, while at the same value of the velocity, the conductivity is lower for higher gas saturation. At high saturations and conductivities the relation does not yield realistic values of the velocities, because the curves are generated by taking the conductivity as the independent variable, and beyond a given threshold the conductivity values are not compatible with high gas saturation.

Figure 3

Figure 4

Figure 5 displays the P-wave phase velocity (a) and the dissipation factor (b) as a function of gas saturation and three values of the clay content. As can be seen, the quality factor has a maximum at 8 % gas saturation in the absence of clay content and the peak moves to higher saturations for increasing clay content.

Figure 5

The conductivity can be related to the hydraulic permeability through the porosity. Figure 6 shows the permeability as a function of conductivity for a clean sandstone (0) and pure shale (1). As expected, the conductivity increases with increasing permeability, since the electrolytic conduction of ions increases with permeability.

Figure 6

We obtain in Appendix D the electromagnetic Green's function and indicate how to obtain the traveltime of the first arrival. This is needed to perform, for instance, traveltime tomography (Michelini, 1995; Lee et al., 2002; Brauchler et al., 2003; Lee and Uchida, 2005). The Green function for $\sigma = 0.2$ S/m is given in Figure 7, where the signals at two receivers are shown. Note that the abscissa is the logarithm of time. This means that at earlier times the signal is very steep and then decays smoothly. The peak times, t_p, are 6.28 μs and 628 μs, respectively. Diffusion fields resemble waves in a log time scale. A test of the modeling algorithm is displayed in Figure 8, where the dots correspond to the numerical solution. The medium is homogeneous with $\sigma = 0.2$

S/m and $\mu_0 = 4\,\pi\,10^{-7}$ H/m (magnetic permeability of vacuum). The number of grid points are $n_x = n_z = 315$ and the grid spacing $dx = dz = 2.5$ m. The computations use $b = 1.2 \times 10^7$/s and $M = 14000$ at 1 s propagation time (these are maximum values) (see Appendix B). The same solution can be obtained with $b = 780000$/s and $M = 3500$, i.e., less computer time, using $dx = dz = 10$ m, at the expense of a coarser grid. The numerical solver needs to be more accurate than in the seismic case, since the peak is located at 0.3 ms, while the signal still decays with a finite amplitude at 1 s propagation time, i.e., the solver has to capture the solution till 3000 times the onset time.

Figure 7

Figure 8

Let us consider a realistic example, with a regular numerical mesh with grid spacing $dx = dz = 2.5$ m The model is a sandstone aquifer with shale intrusions, embedded in a shale formation. The properties at each grid point in the sandstone layer are obtained as follows:

i) Set the porosity ϕ, clay content C and saturation S_g;

ii) Use equation (1) to obtain the conductivity;

iii) Obtain the seismic velocities at f_0 using equations (3);

iv) Obtain the quality factor Q_0 from equation (20) and set $Q_0^{(1)} = Q_0$ and calculate $Q_0^{(2)}$ from equation (19). The relaxation times are obtained using equations (32);

v) Compute the density from equation (7).

It is assumed that $\mathcal{A} = 3$ in equation (9) and $2\pi\tau_0 f_0 = 1$, where $f_0 = 150$ Hz. We consider the model shown in Figure 9, which shows the porosity (a), clay content (b), permeability (c) and gas saturation after the injection (d). Before the injection, the layer is fully saturated with water ($S_g = 0$). The conductivity before and after the injection is shown in Figure 10. On the other hand, Figure 11 displays the seismic properties of the same model, before and after the injection.

Both, the EM and seismic meshes have 315 $\times$ 315 points with square cells of $dx = dz = 2.5$ m size. The source time history is

$$h(t) = \left(u - \frac{1}{2}\right) \exp(-u), \quad u = \left[\frac{\pi(t - t_s)}{T}\right]^2, \tag{14}$$

where T is the period of the wave and we take $t_s = 1.4T$. The peak frequency is $f_p = 1/T$. The simulations use an explosion as a source [$f_{xx} = f_{zz}$ in equations (25) and (26)] and a central frequency $f_p = 150$ Hz. The time step of the Runge-Kutta algorithm is 0.1 ms.

Figure 12 shows the electromagnetic simulation before and after the injection (solid and dashed curves, respectively, in c) and d). As can be seen, the traveltimes after the injection are lower due to the higher resistivity of the layer partially saturated with carbon dioxide. The seismic (viscoelastic) simulations are shown in Figure 13 and in this case the traveltimes after the injection are higher than the traveltimes obtained for a water saturated aquifer.

In the upper part of the aquifer, the gas saturation after the injection is about 20 to 40 % (see Figure 9d). The conductivity has been reduced by a factor two, approximately from 1.6 S/m to 0.8 S/m (see Figure 10), which generates a maximum traveltime difference (at receiver 15) of nearly 3 ms, before and after injection. This difference and the related conductivity contrast should be significant for a tomography inversion algorithm to detect the presence of gas (e.g., Lee and Uchida, 2005).

In the seismic case, the differences in P-wave velocity range from 100 to 200 m/s (Figures 11c and 11d) and P-wave quality-factor values are less than 50 (Figure 11g). These differences in the properties of the medium can safely be detected by means of traveltime and attenuation tomography (Michelini, 1995; Rossi et al. 2007).

The combined use of traveltime and attenuation tomographies provides velocity-Q-factor sections (Rossi et al., 2007). Attenuation has been recognised as a significant seismic indicator, which is not only useful for amplitude analysis and improving resolution, but also to obtain information on lithology, saturation (fluid type), permeability and pore pressure (e.g., Carcione and Gangi, 2000).

Figure 9

Figure 10

Figure 11

Figure 12

Figure 13

5 Conclusions

Time-lapse surveys are essential to detect and monitor the presence of CO_2 in geological formations. The success of this process is subject to a correct description of the physical properties of the CO_2 bearing rocks and use of integrated geophysical methods. We use the White/CRIM relation between seismic velocity and electrical conductivity, which has been successfully tested with well-log data. This integrated model constitutes a porous description of the geological formation, where grain properties, fluid types, porosity, clay content and permeability are explicitly considered, to obtain the electrical conductivity, seismic velocities and seismic quality factors.

Then, we compute the magnetic-field time histories and synthetic seismograms corresponding to a geological model of CO_2 partial saturation, based on a cross-hole source-receiver configuration, and obtain traveltime picks (first arrival versus receiver locations), which are the basis for electromagnetic and seismic tomography. The computed fields before and after CO_2 injection show the expected differences, i.e., higher traveltimes in the electromagnetic case and lower traveltimes in the seismic case. Further research involves the use of various inversion techniques to obtain the location of the CO_2 bubble.

Acknowledgement: This work was supported by projects CO2CARE and QUEST.

References

Alavian, S. A., and Whitson, C. H., 2011. Numerical modeling CO2 injection in a fractured chalk experiment. Journal of Petroleum Science and Engineering, 77, 172-182.

Arts, R., Eiken, O., Chadwick, R. A., Zweigel, P., Van der Meer, L., Zinszner, B., 2004. Monitoring of CO2 injected at Sleipner using time-lapse seismic data. Energy, 29, 1383-1392.

Bourgeois, B., Rohmer, J., and Girard, J.-F., 2009. Numerical modelling of the time-lapse EM response of a CO2 injection in a deep saline aquifer using metallic casings for the current injection, AAPG/SEG/SPE Hedberg conference, "Geological carbon sequestration: Prediction and verification", Vancouver, Canada.

Brauchler, R., Liedl, R., Dietrich, P., 2003. A travel time based hydraulic tomographical approach. Water Resour. Res. 39, 1370, doi:10.1029/2003WR002262.

Carcione, J. M., 2006. A spectral numerical method for electromagnetic diffusion. Geophysics 71, I1-I9.

Carcione, J. M., 2007. Wave Fields in Real Media. Theory and numerical simulation of wave propagation in anisotropic, anelastic, porous and electromagnetic media, 2nd edition, Elsevier.

Carcione, J. M., 2010. Simulation of electromagnetic diffusion in anisotropic media. Progress In Electromagnetics Research B (PIER B) 26, 425-450.

Carcione, J. M., and Gangi, A., 2000. Non-equilibrium compaction and abnormal pore-fuid pressures: effects on seismic attributes, Geophys. Prosp 48, 521-537.

Carcione, J. M., Gurevich, B. and Cavallini, F., 2000, A generalized Biot-Gassmann model for the acoustic properties of shaley sandstones. Geophys. Prosp. 48, 539-557.

Carcione, J. M., Helle, H. B., and Pham, N. H., 2003. White's model for wave propagation in partially saturated rocks: Comparison with poroelastic numerical experiments. Geophysics 68, 1389-1398.

Carcione, J. M., Kosloff, D., and Kosloff, R., 1988. Wave propagation simulation in a linear viscoelastic medium. Geophys. J. Roy. Astr. Soc. 95, 597-611.

Carcione, J. M., Picotti, S., Gei, D., and Rossi, G., 2006. Physics and seismic modeling for monitoring CO2 storage. Pure and Applied Geophysics 163, 175-207.

Carcione, J. M., Ursin, B., and Nordskag, J. I., 2007. Cross-property relations between electrical conductivity and the seismic velocity of rocks. Geophysics 72, E193-E204.

Carslaw, H. S., and Jaeger, J. C., 1959. Conduction of heat in solids, Clarendon Press.

Christensen, N. B., Sherlock, D., Dodds, K., 2006. Monitoring CO2 injection with cross-hole electrical resistivity tomography. Exploration Geophysics 37, 44-49.

David, E. C., and Zimmerman, R. W., 2011, Elastic moduli of solids containing spheroidal pores. Int. J. Eng. Sci. 49, 544-560.

Giese, R., Henninges, J., Lüth, S., Morozova, D., Schmidt-Hattenberger, C., Würdemann, H., Zimmer, M., Cosma, C., Juhlin, C., and CO_2 SINK Group, 2009. Monitoring at the CO_2 SINK site: A concept integrating geophysics, geochemistry and microbiology. Energy Procedia 1, 2251-2259.

Hagrey, S. A. al, 2010. CO_2 plume modeling in deep saline reservoirs by 2D ERT in boreholes. The Leading Edge 30, 24-33.

Hashin, Z., and Shtrikman, S., 1963. A variational approach to the theory of the elastic behaviour of multiphase materials. J. Mech. Phys. Solids 11, 127-140.

Hoversten, G. M., Cassassuce, F., Gasperikova, E., Newman, G. A., Chen, J., Rubin, Y., Hou, Z., and Vasco, D., 2006. Direct reservoir parameter estimation using joint inversion of marine seismic AVA and CSEM data. Geophysics 71, C1-C13.

Hoversten, G. M., Milligan, P., Byun, J., Washbourne, J., Knauerzz, L. C., and Harnesszz, P., 2004. Crosswell electromagnetic and seismic imaging: An examination of coincident surveys at a steam flood project. Geophysics 69, 406-414.

Kachanov, M., Sevostianov, I., and Shafiro, B., 2001. Explicit cross-property correlations for porous materials with anisotropic microstructures. Journal of the Mechanics and Physics of Solids 49, 1-25.

Kosloff, D, and Kosloff, R., 1986. Absorbing boundaries for wave propagation problems. J. Comput. Phys. 63, 363-376.

Lee, T. J., Suh, J. H., Kim, H. J., Song, Y., and Lee, K. H., 2002. Electromagnetic traveltime tomography using an approximate wavefield transform. Geophysics 67, 68-76.

Lee, T. J., and Uchida, T., 2005. Electromagnetic traveltime tomography: Application for reservoir characterization in the Lost Hills oil field, California. Geophysics 70, G51-G58.

Lei, X., and Xue, Z., 2009. Ultrasonic velocity and attenuation during CO_2 injection into water-saturated porous sandstone: Measurements using difference seismic tomography. Physics of the Earth and Planetary Interiors 176, 224-234.

Le Ravalec, M., and Gueguen, Y., 1996, High- and low-frequency elastic moduli for a saturated porous/cracked rock-differential self-consistent and poroelastic theories. Geophysics 61, 1080-1094.

Li, H., and Zhang, J., 2011, Analytical approximations of bulk and shear moduli for dry rock based on the differential effective medium theory, Geophys. Prosp., doi: 10.1111/j.1365-2478.2011.00980.x

Mavko, G., Mukerji, T., and Dvorkin, J., 1998. The rock physics handbook: tools for seismic analysis in porous media, Cambridge Univ. Press.

Michelini A., 1995. An adaptive-grid formalism for traveltime tomography. Geoph. J. Int.. 121, 489-510.

Norman, T., Alnes, H., Christensen, O., Zach, J. J., Eiken, O., and Tjaland, E., 2008. Planning time-lapse CSEM-surveys for joint seismic-EM monitoring of geological carbon dioxide injection, EAGE CO2 Geological Storage Workshop - Budapest, Hungary,

Oristaglio, M. L. and Hohmann, G. W., 1984. Diffusion of electromagnetic fields into a two-dimensional earth: A finite-difference approach. Geophysics 49, 870-894.

Picotti, S., Carcione, J. M., Rubino, G., Santos, J. E., and Cavallini, F., 2010, A viscoelastic representation of wave attenuation in porous media. Computer & Geosciences 36, 44-53.

Rossi, G., Gei, D., Böhm, G., Madrussani, G., and Carcione, J. M., 2007, Attenuation tomography: An application to gas-hydrate and free-gas detection, Geophysical Prospecting 55, 655-669.

Schön, J. H., 1996. Physical properties of rocks, Handbook of geophysical exploration, Pergamon Press.

White, J. E., 1975. Computed seismic speeds and attenuation in rocks with partial gas saturation. Geophysics 40, 224-232.

Wilt, M. J., Alumbaugh, D. L., Morrison, H. F., Becker, A., Lee, K. H., and Deszcz-Pan, M., 1995, Crosswell electromagnetic tomography - System design considerations and field results. Geophysics 60, 871-885.

Yu, L., and Edwards, R. N., 1997. On crosswell diffusive time-domain electromagnetic tomography. Geophysical Journal International 130, 449-459.

A White's mesoscopic model including S-wave dissipation

White (1975) assumed spherical patches much larger than the grains but much smaller than the wavelength. He developed the theory for a gas-filled sphere of porous medium of radius r_0 located inside a water-filled sphere of porous medium of outer radius r_1 ($r_0 < r_1$). The saturation of gas is

$$S_g = \frac{r_0^3}{r_1^3} \quad \text{and} \quad S_b = 1 - S_g \tag{15}$$

is the brine saturation.

Assuming that the dry-rock and grain moduli and permeability, κ, of the different regions are the same, the complex bulk modulus as a function of frequency is given by

$$K = \frac{K_\infty}{1 - K_\infty W}, \tag{16}$$

where K_∞ is a – high frequency – bulk modulus when there is no fluid flow between the patches, and W is a compliance proportional to the permeability. The explicit expressions are not given here for brevity and can be found in Mavko et al. (1998), Carcione et al. (2003) and Picotti et al. (2010). For values of the gas saturation higher than 52 %, or values of the water saturation between 0 and 48 %, the theory is not rigorously valid. Another limitation to consider is that the size of gas pockets should be much smaller than the wavelength.

Clay content also affects the permeability. Carcione et al. (2000) derived a model of permeability as a function of clay content. They assumed that a shaly sandstone is composed of a sandy matrix and a shaly matrix with partial permeabilities

$$\kappa_q = \frac{R_q^2 \phi^3}{45(1-\phi)^2(1-C)} \quad \text{and} \quad \kappa_c = \frac{R_c^2 \phi^3}{45(1-\phi)^2 C}, \tag{17}$$

where R_q and R_c denote the average radii of sand and clay particles, respectively. Assuming that permeability is analogous to the inverse of the electrical resistance, the average permeability of the shaly sandstone is given by

$$\frac{1}{\kappa} = \frac{1-C}{\kappa_q} + \frac{C}{\kappa_c} = \frac{(1-\phi)^2}{A\phi^3}\left[(1-C)^2 + C^2B^2\right], \tag{18}$$

where $A = R_q^2/45$ and $B = R_q/R_c$ or can be assumed as empirical parameters.

Since White's theory does not predict any shear dissipation, we assume that the complex modulus $\boldsymbol{\mu}$ is described by a Zener element having a peak frequency f_0 and a minimum quality factor given by

$$Q_0^{(2)} = \frac{\mu_m}{\mathrm{Re}[K(f_0)]} Q_0, \tag{19}$$

where Q_0 is the quality factor associated with K at f_0, i.e.,

$$Q_0 = Q(f_0) = \frac{\mathrm{Re}[K(f_0)]}{\mathrm{Im}[K(f_0)]}. \tag{20}$$

The model for the anelastic dilatations is based on a poroelastic model, but the viscoelastic behavior of the shear waves is incorporated into the modeling in an ad hoc manner. The problem is the lack of a mesoscopic theory for shear deformations, i.e., something similar to White's model. To model the amount of loss related to the shear motions, we assume that the stiffer the medium the higher the quality factor (relation (19)), i.e., if the modulus increases the attenuation decreases and vice versa. However, the Zener model is consistent with White's theory, since both models describe anelasticity in the form of a relaxation peak in the frequency domain. Picotti et al. (2010) show that White's model can be represented by a Zener mechanical element.

Then, the dimensionless modulus is given by equation (31), and

$$\boldsymbol{\mu} = \mu M_2 \tag{21}$$

where μ and M_2 are given in the next section. Note that Q_0 depends on gas saturation. The frequency f_0 is taken in the seismic frequency range in this work, particularly, equal to the source dominant frequency.

B Electromagnetic modeling

Equation (12) has the form $\partial_t H_y = \mathcal{O} H_y$, with $\mathcal{O} = [(\sigma^{-1} H_{y,x})_{,x} + (\sigma^{-1} H_{y,z})_{,z}]/\mu_0$. The eigenvalue equation in the complex λ-domain ($\lambda = -\mathrm{i}\omega$), corresponding to operator $\mathcal{O}$, is $\lambda[\lambda + D(k_x^2 + k_z^2)] = 0$, where ω is the frequency and $D = 1/(\mu_0 \sigma)$. The eigenvalues are therefore zero and real and negative, and the maximum (Nyquist) wavenumber components are $k_x = \pi/dx$ and $k_z = \pi/dz$ for the grid spacings dx and dz. The solution of equation (12) can be obtained as

$$H_y(t) = \sum_{k=0}^{M} c_k \exp(-bt) I_k(tR) Q_k(\mathcal{O}/b + 1) H_{y0}, \tag{22}$$

where H_{y0} is a discrete spatial delta function applied at the source location, b is the absolute value of the largest eigenvalue of $\mathcal{O}$, I_k is the modified Bessel function of order k, $c_0 = 1$ and $c_k = 2$ for $k \neq 0$, and Q_k are modified Chebyshev polynomials. The value of b is equal to $(\pi^2/D)(1/dx^2 + 1/dz^2)$, while R should be chosen slightly larger than b. The maximum polynomial order M should be $O(\sqrt{bt})$. It can be shown that $M = 6\sqrt{bt}$ is enough to obtain stability and accuracy (Carcione, 2006).

The algorithm is a three-level scheme, since it uses the recurrence relation of the Chebyshev polynomials. The solution is obtained at one large time step T. Results at smaller time levels, $t < T$, to compute time histories at specified points of the grid, do not require significant computational effort, since the terms involving the spatial derivatives do not depend on the time variable and are calculated in any case. Only the coefficients $\exp(-bt)I_k(tR)$ are time dependent, such that additional sets of Bessel functions need to be computed. The intermediate time levels can be defined on a logarithm scale to better capture the peak of the first arrival (see Appendix D).

The boundaries of the mesh may produce wraparounds due to the periodic properties of the Fourier method. We use the classical damping approach to avoid these non-physical artifacts (Kosloff and Kosloff, 1986; Carcione, 2007). The method simply requires to modify the differential operator as $\mathcal{O} \to \mathcal{O} - o$ in the absorbing strips around the mesh, where o is different from zero at narrow strips surrounding the mesh. Its value has to be optimized in such a way that the diffusion field agrees with an analytical solution at times much larger than the peak of the signal (see Appendix D).

C Viscoelastic differential equations

The time-domain equations for propagation in a heterogeneous viscoelastic medium can be found in Carcione (2007). The anelasticity is described by the standard linear solid, also called the Zener model, that gives relaxation and creep functions in agreement with experimental results.

The two-dimensional velocity-stress equations for anelastic propagation in the (x, z)-plane, assigning one relaxation mechanism to dilatational anelastic deformations ($\nu = 1$) and one relaxation mechanism to shear anelastic deformations ($\nu = 2$), can be expressed by

i) Euler-Newton's equations:

$$\dot{v}_x = \frac{1}{\rho}(\sigma_{xx,x} + \sigma_{xz,z}) + f_x, \tag{23}$$

$$\dot{v}_z = \frac{1}{\rho}(\sigma_{xz,x} + \sigma_{zz,z}) + f_z, \tag{24}$$

where v_x and v_z are the particle velocities, σ_{xx}, σ_{zz} and σ_{xz} are the stress components, ρ is the density and f_x and f_z are the body forces.

ii) Constitutive equations:

$$\dot{\sigma}_{xx} = k(v_{x,x} + v_{z,z} + e_1) + \mu(v_{x,x} - v_{z,z} + e_2) + f_{xx}, \tag{25}$$

$$\dot{\sigma}_{zz} = k(v_{x,x} + v_{z,z} + e_1) - \mu(v_{x,x} - v_{z,z} + e_2) + f_{zz}, \tag{26}$$

$$\dot{\sigma}_{xz} = \mu(v_{x,z} + v_{z,x} + e_3) + f_{xz}, \tag{27}$$

where e_1, e_2 and e_3 are memory variables, f_{ij} are external sources, and k and μ are the unrelaxed (high-frequency) bulk and shear moduli, respectively, given by in the next section.

iii) Memory variable equations:

$$\dot{e}_1 = \left(\frac{1}{\tau_\epsilon^{(1)}} - \frac{1}{\tau_\sigma^{(1)}}\right)(v_{x,x} + v_{z,z}) - \frac{e_1}{\tau_\sigma^{(1)}}, \tag{28}$$

$$\dot{e}_2 = \left(\frac{1}{\tau_\epsilon^{(2)}} - \frac{1}{\tau_\sigma^{(2)}}\right)(v_{x,x} - v_{z,z}) - \frac{e_2}{\tau_\sigma^{(2)}}, \tag{29}$$

$$\dot{e}_3 = \left(\frac{1}{\tau_\epsilon^{(2)}} - \frac{1}{\tau_\sigma^{(2)}}\right)(v_{x,z} + v_{z,x}) - \frac{e_3}{\tau_\sigma^{(2)}}, \tag{30}$$

where $\tau_\sigma^{(\nu)}$ and $\tau_\epsilon^{(\nu)}$ are material relaxation times, corresponding to dilatational ($\nu = 1$) and shear ($\nu = 2$) deformations.

C.1 Propagation properties

The complex moduli associated with bulk and shear deformations are the Zener moduli,

$$M_\nu = \frac{\tau_\sigma^{(\nu)}}{\tau_\epsilon^{(\nu)}}\left(\frac{1 + \mathrm{i}\omega\tau_\epsilon^{(\nu)}}{1 + \mathrm{i}\omega\tau_\sigma^{(\nu)}}\right), \quad \nu = 1, 2 \tag{31}$$

where $\mathrm{i} = \sqrt{-1}$, such that the relaxation times can be expressed as

$$\tau_\epsilon^{(\nu)} = \frac{\tau_0}{Q_0^{(\nu)}}\left(\sqrt{Q_0^{(\nu)^2} + 1} + 1\right), \quad \tau_\sigma^{(\nu)} = \tau_\epsilon^{(\nu)} - \frac{2\tau_0}{Q_0^{(\nu)}}, \tag{32}$$

where τ_0 is a relaxation time such that $1/\tau_0$ is the center frequency of the relaxation peak and $Q_0^{(\nu)}$ are the minimum quality factors. The complex (viscoelastic) bulk and shear moduli are

$$\bar{K} = kM_1 \quad \text{and} \quad \boldsymbol{\mu} = \mu M_2. \tag{33}$$

In order to obtain μ and k, we express the P and S viscoelastic phase velocities as

$$c_P = \left[\mathrm{Re}\left(\frac{1}{v_P}\right)\right]^{-1} \quad \text{and} \quad c_S = \left[\mathrm{Re}\left(\frac{1}{v_S}\right)\right]^{-1}, \tag{34}$$

where

$$v_P = \sqrt{\frac{1}{\rho}\left(\bar{K} + \frac{4}{3}\boldsymbol{\mu}\right)} \quad \text{and} \quad v_S = \sqrt{\frac{\boldsymbol{\mu}}{\rho}}, \tag{35}$$

respectively. First, we obtain μ as

$$\mu = \mu_m \left[\mathrm{Re}\sqrt{\frac{1}{M_2(f_0)}}\right]^2, \tag{36}$$

assuming $\mu_m = \rho c_S^2(f_0)$, and k is computed by solving

$$\mathrm{Re}\sqrt{\frac{\rho}{kM_1(f_0) + 4\mu M_2(f_0)/3}} - \frac{1}{c_P(f_0)} = 0. \tag{37}$$

D Electromagnetic Green's function and traveltime picking

Traveltime tomography is based on the first arrival at each receiver (e.g., Michelini, 1995). To illustrate the physics we consider a solution of equation (12) in the case of isotropic homogeneous media. The Green function corresponding to equation (38), with $J_x = J_z = 0$, and a magnetic source

$$M_y(x, y, t) = M_0\delta(x)\delta(z)[1 - H(t)], \tag{38}$$

is the solution of

$$\partial_t H_y = D\Delta H_y + M_0\delta(x)\delta(z)\delta(t), \tag{39}$$

where M_0 defines the direction and the strength of the source, and

$$D = \frac{1}{\mu_0\sigma} \tag{40}$$

is the diffusivity. Equation (39) has the following solution (Green's function):

$$H_y(r, t) = \frac{M_0}{(4\pi Dt)^{N/2}} \exp[-r^2/(4Dt)], \tag{41}$$

where N is the space dimension ($N = 2$ in this work), and

$$r = \sqrt{x^2 + z^2} \tag{42}$$

(Carslaw and Jaeger, 1959; Oristaglio and Hohmann, 1984; Carcione, 2010).

The solution $H_y(t)$ has a maximum at

$$t_p = \frac{r^2}{4D} = \frac{\mu_0 \sigma r^2}{4} \tag{43}$$

[$t_p = r^2/(6D)$ in 3D space]. Then, in a homogeneous medium, the conductivity can simply be obtained as $\sigma = 4t_p/(\mu_0 r^2)$, at a source-receiver distance r. Equation (43) indicates that the diffusion is faster in resistive media. The phase velocity and attenuation factor for planes waves is

$$v_p = 2\sqrt{\frac{\pi f}{\mu \sigma}}, \quad \text{and} \quad \alpha = \sqrt{\pi f \mu_0 \sigma}, \tag{44}$$

respectively, where f is the frequency (e.g., Carcione, 2007); α is the reciprocal of the skin depth and therefore the penetration is less in more conductive media.

In inhomogeneous media we need to perform traveltime tomography (e.g., Brauchler et al., 2003), which is based on the following line integral

$$\sqrt{t_p} = \frac{1}{4} \int_{x_1}^{x_2} \frac{ds}{\sqrt{D}}, \tag{45}$$

where x_1 and x_2 refer to the source and receiver locations, respectively. The procedure is similar to seismic traveltime tomography, where the line integral has the form $t_p = \int ds/v_p$, with v_p the wave velocity (Michelini, 1995). In our case, one has to find the diffusivity (or conductivity) model that minimizes the functional $\sum_i^n (\sqrt{t_i^m} - \sqrt{t_i})^2$, where t_i^m is the measured traveltime and t_i is the ray-tracing (computed) traveltime. The first break is obtained as the time that the first derivative of the field is maximum (Yu and Edwards, 1997). An alternative picking method is given in Lee and Uchida (2005).

Table 1. Elastic and electromagnetic properties.

Medium	K (GPa)	μ (GPa)	ρ (g/cm^3)	R (μm)	η (Pa s)	σ (S/m)
Clay	25	20	2.65	1	–	0.2
Sand grains	39	40	2.65	50	–	0.01
Brine	2.25	0	1.03	–	0.0012	12
CO_2	0.025	0	0.5	–	0.00002	0

$\phi = 25$ %, $r_1 = 10$ cm.

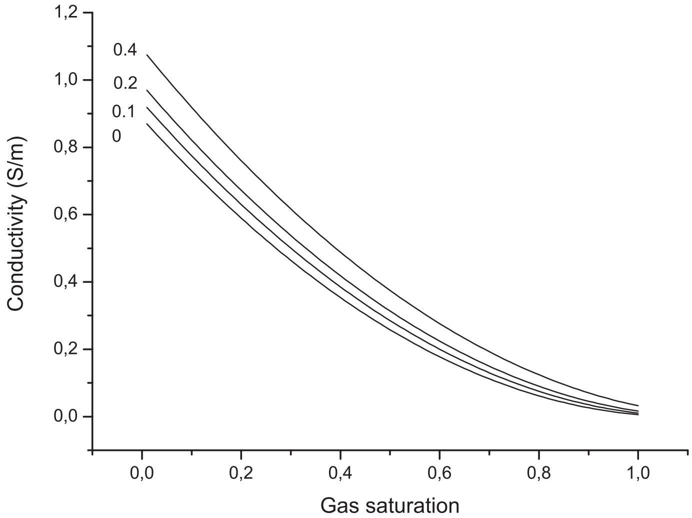

Fig. 1 Rock conductivity as a function of gas saturation. The numbers indicate the clay content.

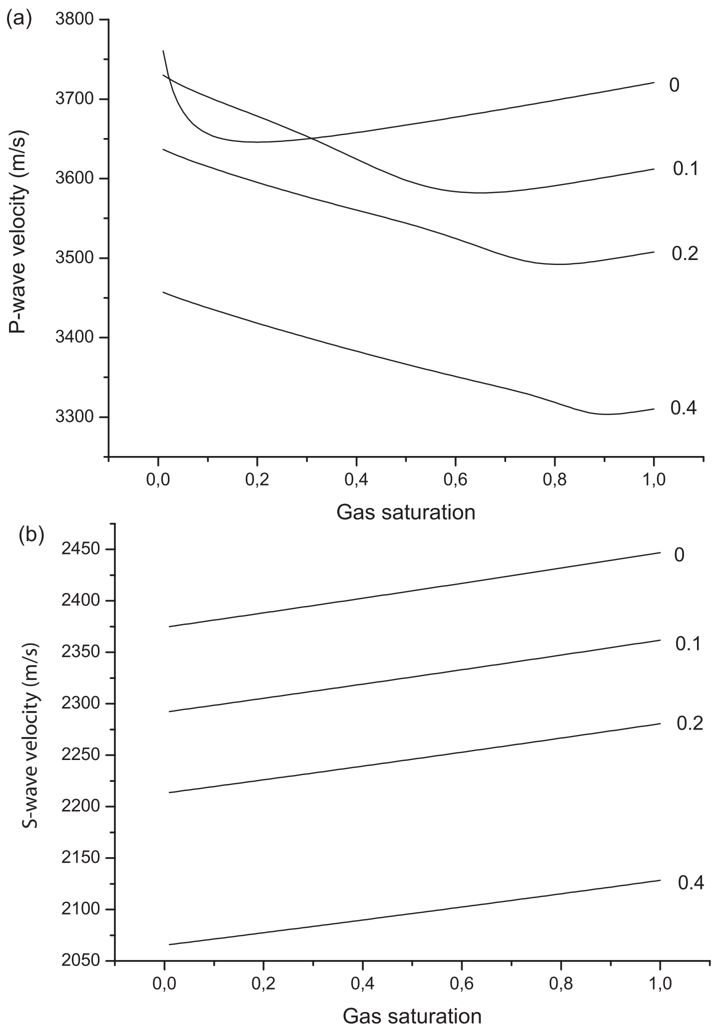

Fig. 2 P-wave (a) and S-wave (b) velocities as a function of gas saturation at 200 Hz. The numbers indicate the clay content.

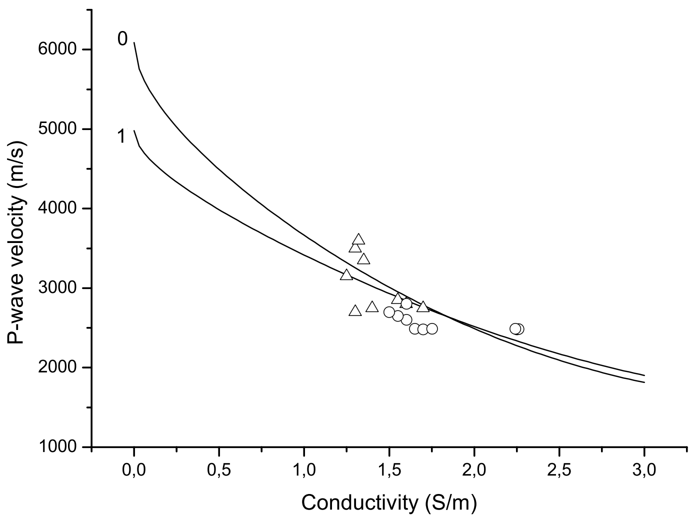

Fig. 3 P-wave velocity as a function of the conductivity, where the brine saturation is 100 %. The numbers indicate the clay content, and the triangles and circles correspond to the sandy and shaly sections of the well.

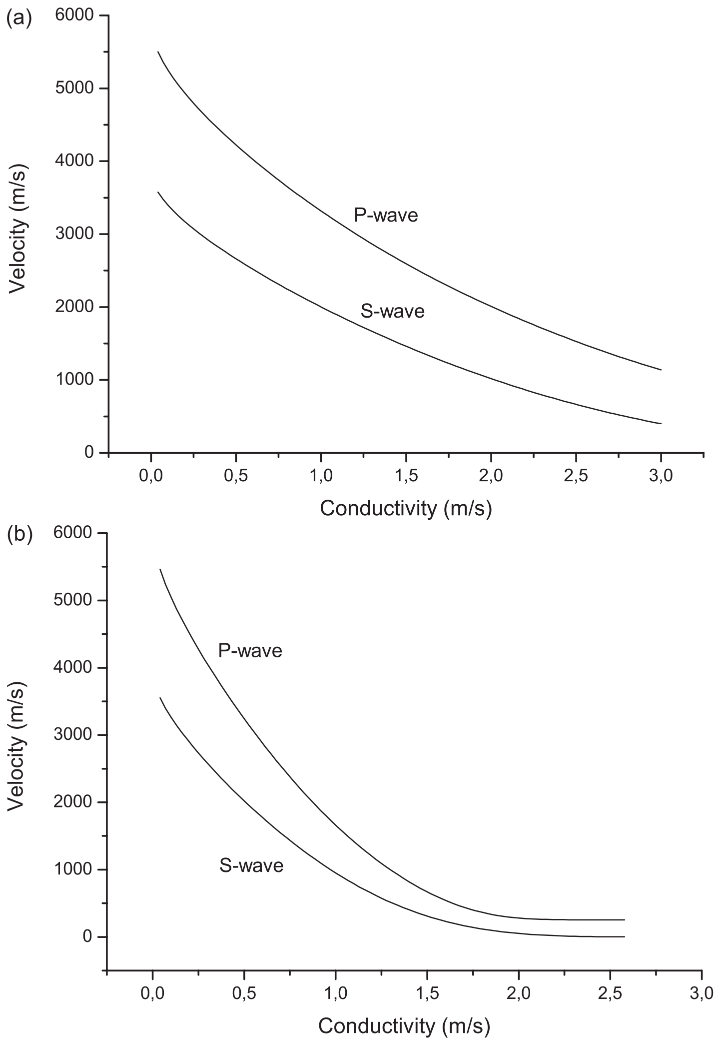

Fig. 4 P- and S-wave velocities as a function of the conductivity at a frequency of 200 Hz. The clay content is $C = 0.2$ and the gas saturation is $S_g = 0.1$ (a) and 0.4 (b).

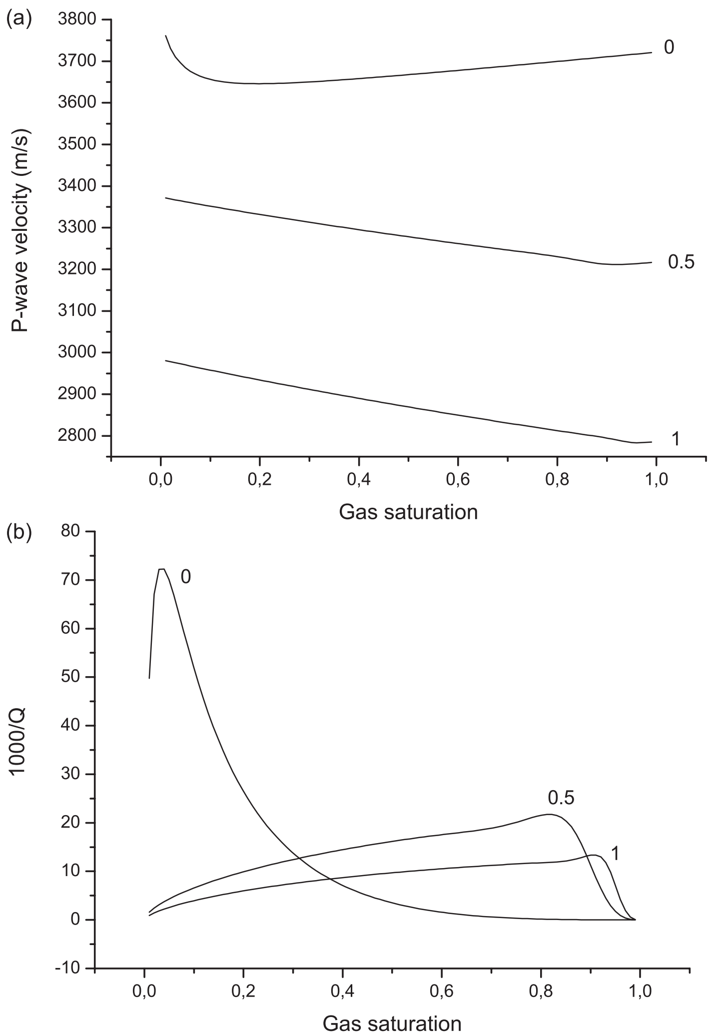

Fig. 5 P-wave velocity (a) and dissipation factor (b) as a function of the saturation for 0, 50 and 100 % clay content. The frequency is 200 Hz.

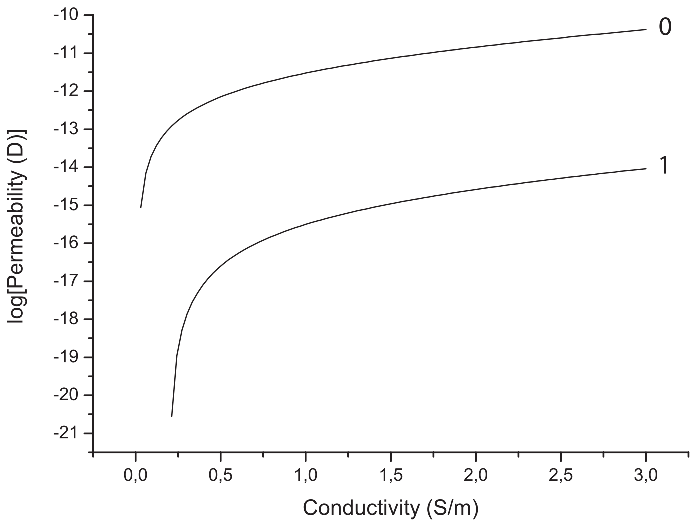

Fig. 6 Permeability as a function of conductivity for C=0 (clean sandstone) and C=1 (shale) (-12 correspond to 1 D).

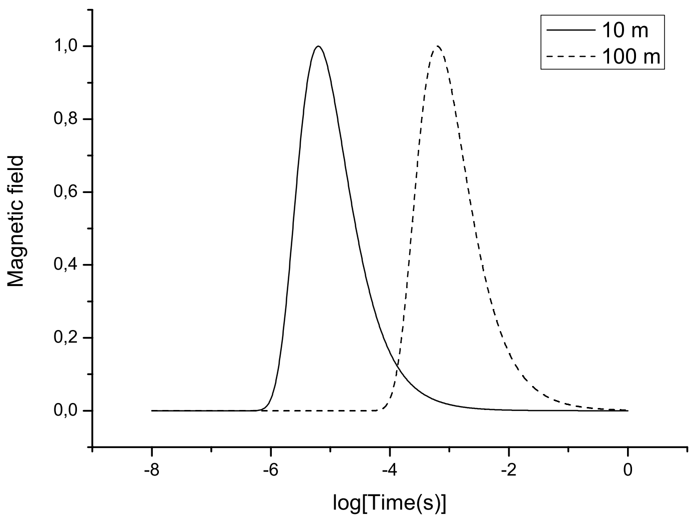

Fig. 7 Electromagnetic Green's function as a function of time at two receivers. The fields are normalized and the signal at 100 m has an amplitude 100 times weaker than the signal at 10 m.

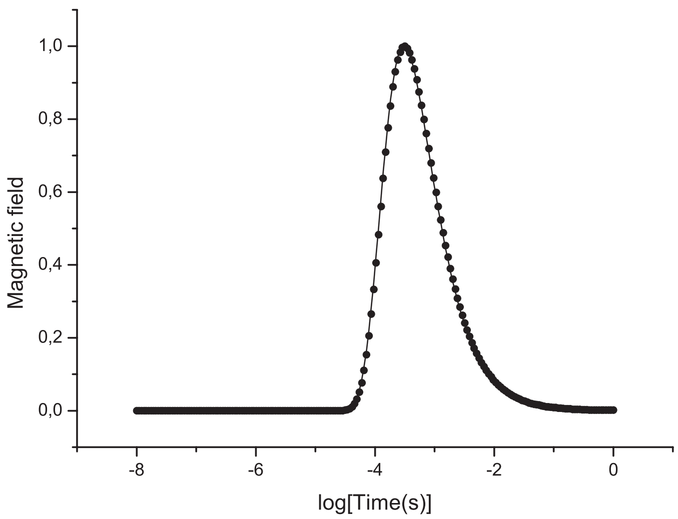

Fig. 8 Comparison between numerical and analytical solutions (normalized) at $(x, z) =$ (50,50) m ($r \approx 70$ m) from the source location (center of the mesh). The solid line corresponds to the analytical solution, obtained from equation (41).

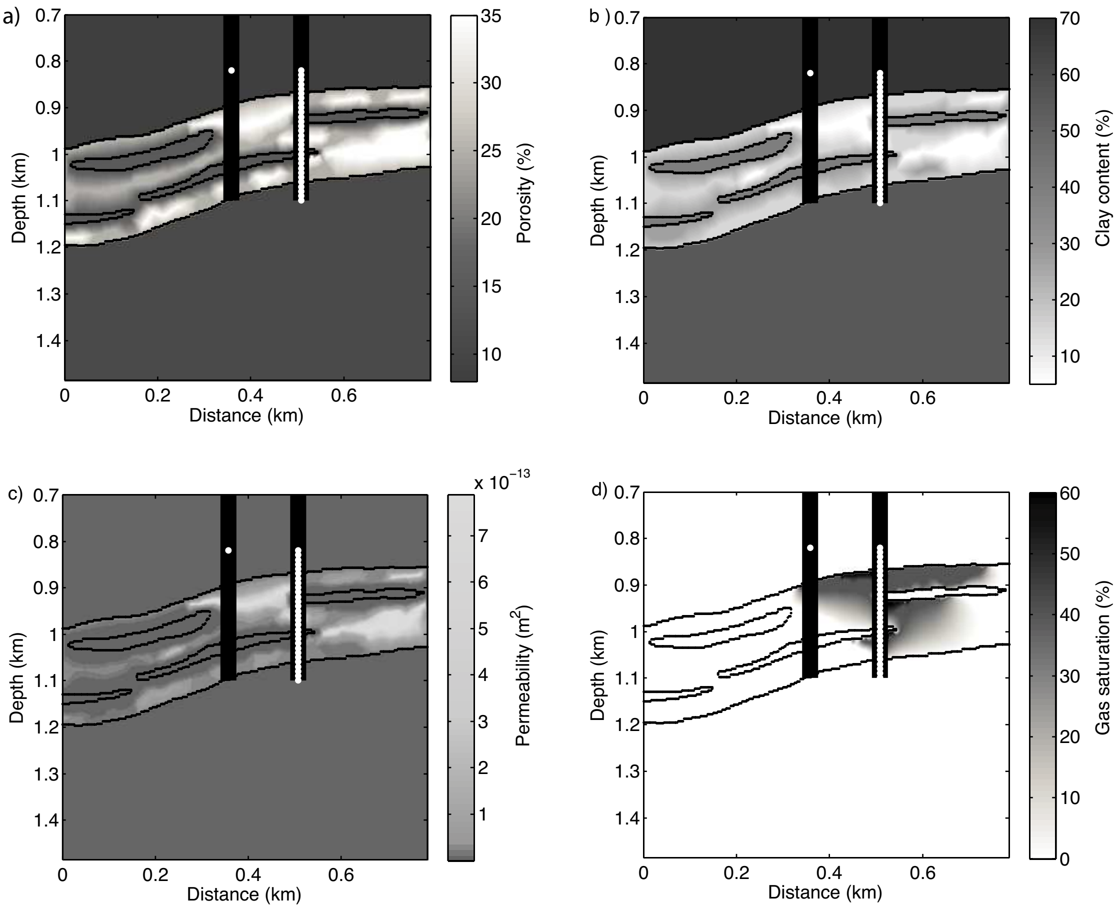

Fig. 9 Porosity (a), clay content (b), permeability (c) and CO_2 saturation after the injection (d). The locations of the source (left) and receiver (right) wells are indicated.

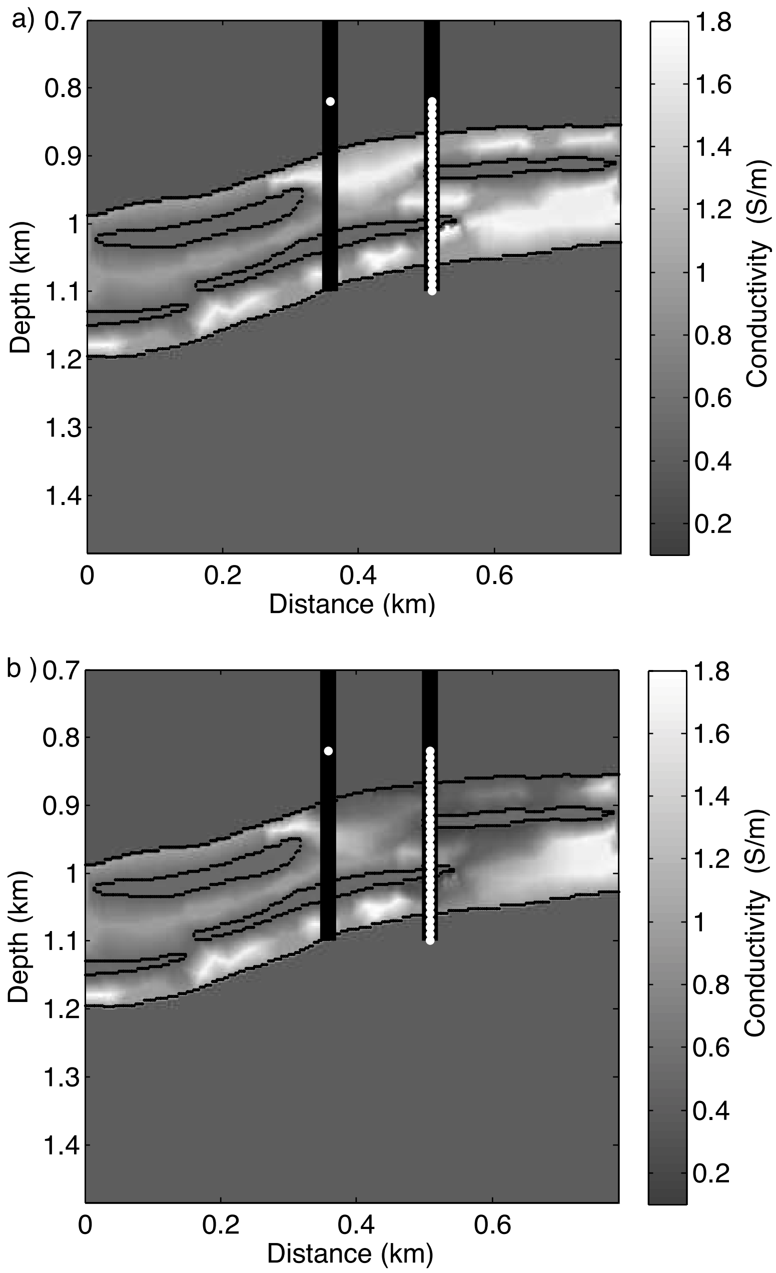

Fig. 10 Conductivity before (a) and after (b) CO_2 injection.

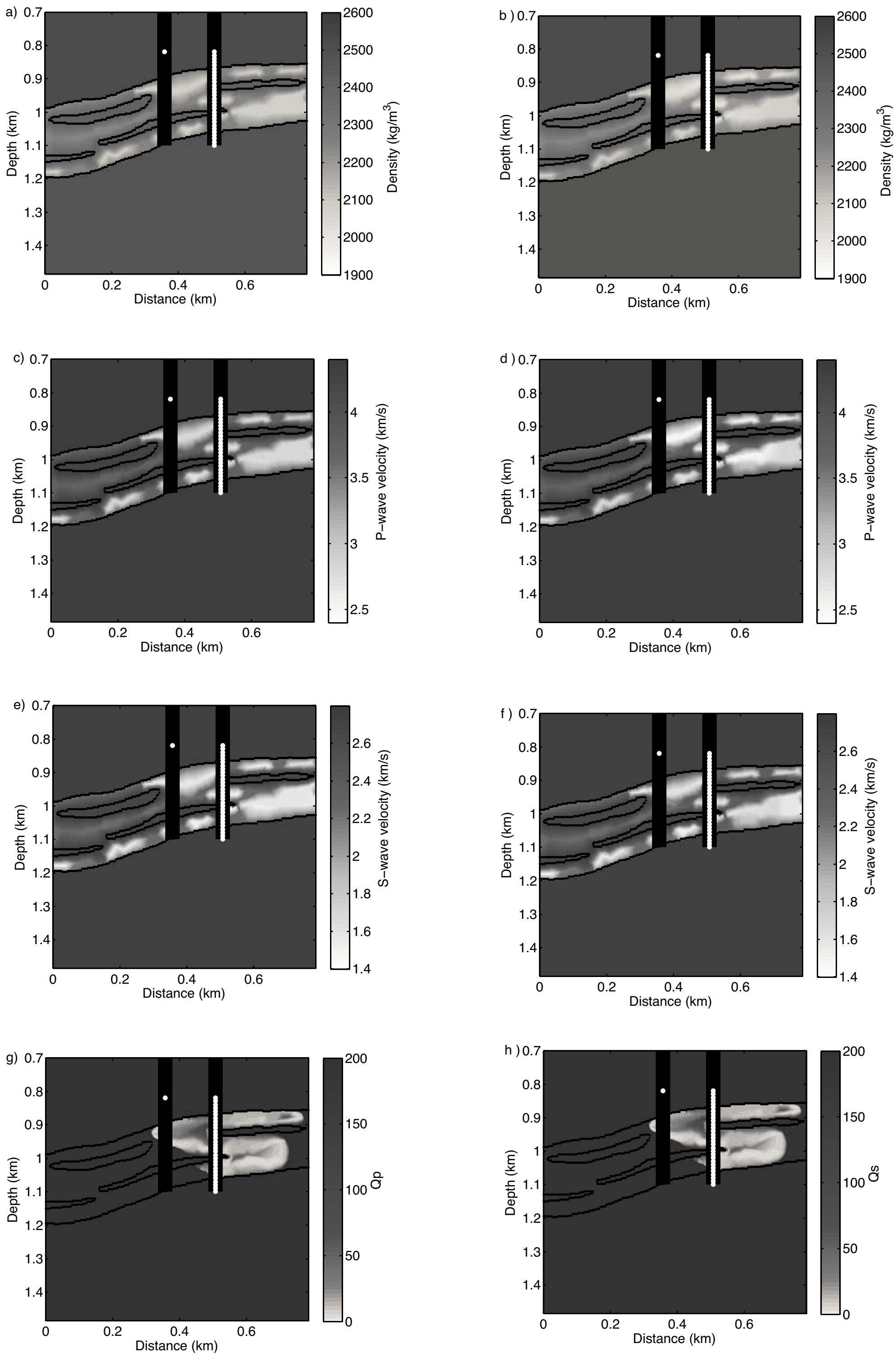

Fig. 11 Panels (a), (c), and (e) show the density, P-wave velocity and S-wave velocity before CO_2 injection, respectively. Panels (b), (d) and (f) show the same properties after CO_2 injection. Panels (g) and (h) show Q_P and Q_S at f_0, respectively, obtained from equation (4), after CO2 injection ($Q_S = Q_0^{(2)}$).

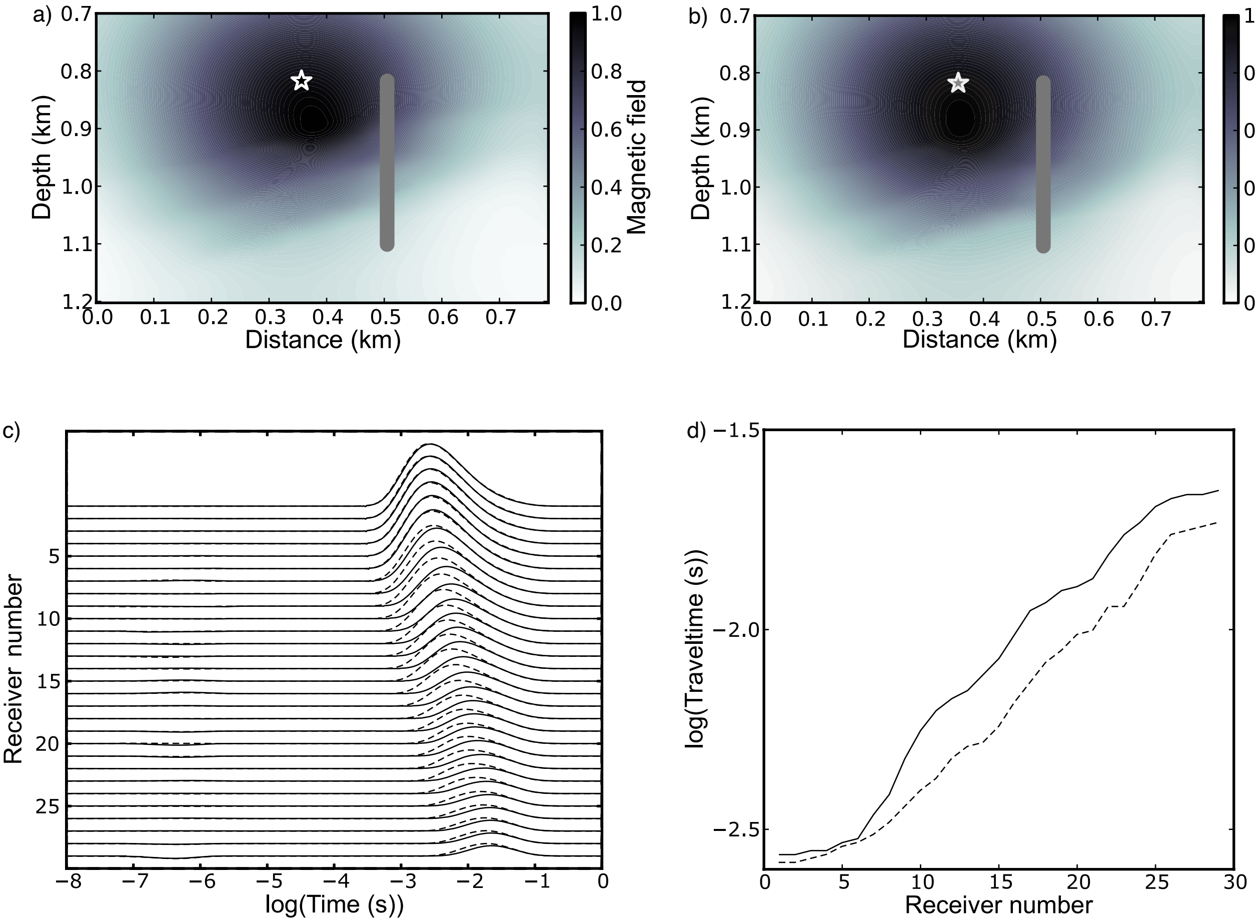

Fig. 12 Snapshots of the normalized magnetic field at 20 ms before (a) and after (b) CO_2 injection. The source and the vertical array of receivers are represented by the star and vertical line, respectively. Panel (c) represents the normalized amplitude variation versus receiver number before and after injection (solid and dashed curves, respectively, and panel (d) shows the traveltime picks before and after injection (solid and dashed curves, respectively).

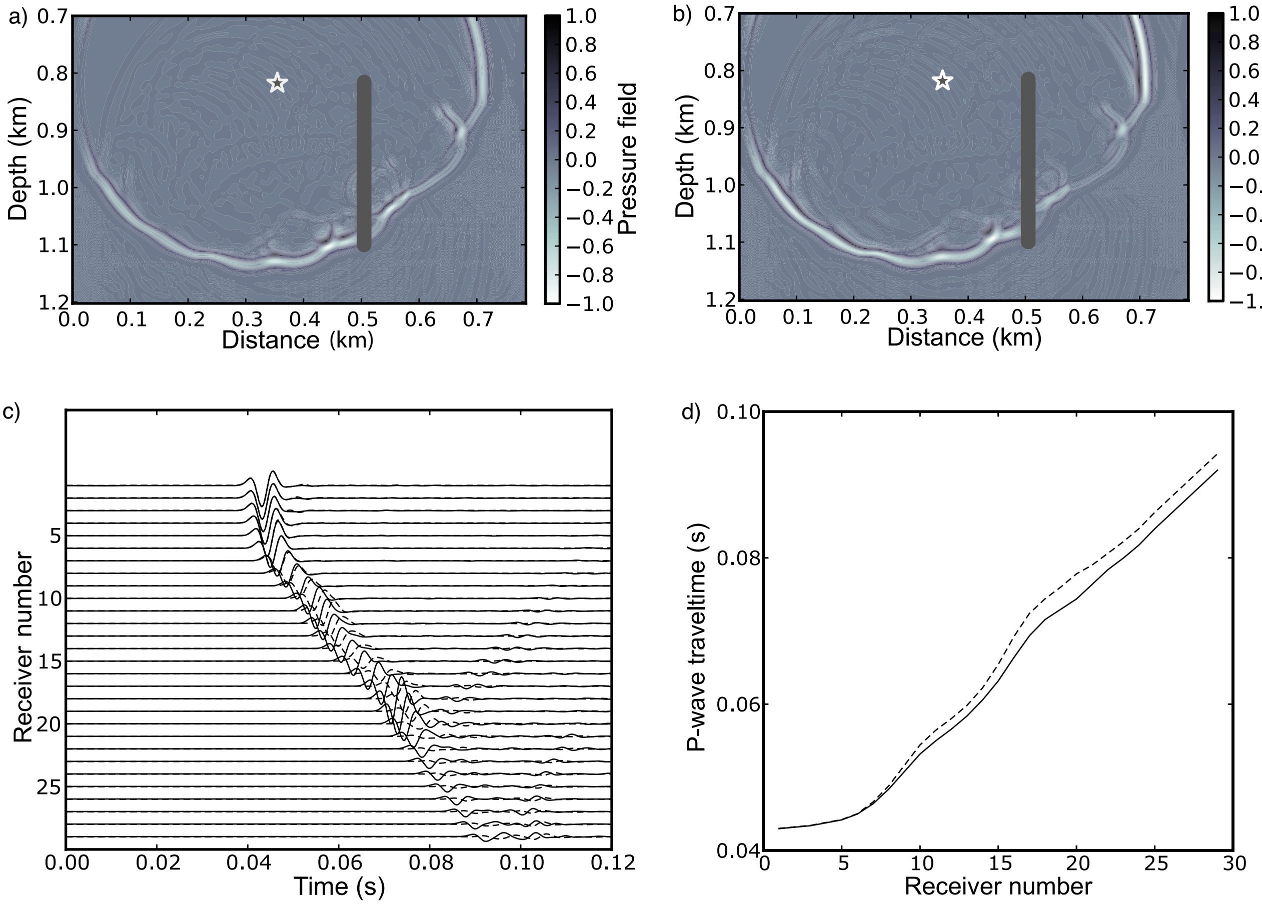

Fig. 13 Snapshot of the normalized pressure field at 90 ms before (a) and after the injection (b). The source and the vertical array of receivers are represented by the red star and vertical line, respectively. Panel (c) represents the normalized amplitude variation versus receiver number before and after injection (solid and dashed curves, respectively, and panel (d) shows the traveltime picks before and after injection (solid and dashed curves, respectively).